RSC Sustainability

ROYAL SOCIETY OF CHEMISTRY

PAPER

View Article Online
View Journal | View Issue

Cite this: *RSC Sustainability*, 2026, **4**, 511

Mechano-stimuli-responsive engineered device mimicking native anisotropy towards tissue regeneration

Samir Das,[a] Sri Medha Juloori,[a] Mainak Swarnakar,[b] Manish Pal Chowdhury[b] and Santanu Dhara *[a]

Tissue-related disorders continue to present critical clinical challenges due to their limited self-repair abilities and rising global incidence. Conventional grafting techniques and implant materials are suffering from significant drawbacks, including immune rejection, donor site morbidity, and lack of bioactivity. Herein, this study explores the development of a smart, biomimetic scaffold that combines a piezoelectric polymer polyvinylidene fluoride (PVDF) with a demineralized extracellular matrix derived from fish scales. The demineralization process effectively removes heavy metal contaminants while preserving the collagen-rich matrix, making it suitable for scaffold applications. PVDF, known for its biocompatibility, flexibility, and electroactive properties, was electrospun at varying concentrations to achieve nanofibrous membranes with tailored anisotropic and electromechanical characteristics. These PVDF nanofibers were layered onto D-FS to create hybrid scaffolds that mimic the hierarchical architecture and dynamic responsiveness of native skeletal tissues. Based on SEM and FTIR analyses, 12% w/v PVDF demonstrated uniform fiber distribution with minimal bead formation. Physico-chemical analyses confirmed its enhanced crystallinity and structural alignment, while electrical assessments demonstrated adequate piezoelectric performance under mechanical stimulation, including device fabrication. Biological evaluations, including the MTT assay, hemolysis analysis, LIVE–DEAD staining, and protein adsorption study, were conducted; the results indicate that C-FS exhibits cytotoxicity, whereas D-FS does not. This work presents a promising strategy for the development of next-generation tissue engineering scaffolds with the potential to eliminate the need for secondary surgeries.

Received 19th June 2025
Accepted 13th November 2025

DOI: 10.1039/d5su00448a

rsc.li/rscsus

Sustainability spotlight

This research illustrates a sustainable materials approach by transforming discarded fish scales, an abundant marine bio-waste, into value-added, collagen-rich scaffolds for regenerative medicine. Through a green demineralization process, the study eliminates heavy metal contaminants while preserving structural anisotropy and bioactivity essential for tissue repair. By integrating electrospun, biodegradable PVDF nanofibers with tailored piezoelectric functionality, the resulting composite mimics native tissue architecture and enables self-powered electrical stimulation. This bioinspired platform not only reduces the dependence on synthetic, non-renewable implants but also promotes circular bioeconomy principles by valorizing waste into clinically relevant, smart biomaterials for next-generation skeletal tissue engineering.

1. Introduction

The global rise in degenerative tissue conditions can be attributed to the aging population and evolving lifestyle habits.[1] Traditional regenerative approaches involving the use of autografts, allografts, xenografts, *etc.* are commonly employed, but they pose significant limitations, including donor site morbidity, immune rejection, and disease transmission.[2] Conventional metallic and ceramic implants offer mechanical strength and biocompatibility, while their bioinert nature and physico-mechanical properties hinder tissue integration and remodelling.[3] Moreover, they fail to replicate the complex anisotropic architecture of native tissues. Emerging strategies focus on engineering smart biomaterials that mimic tissue anisotropy and stimulate ECM niche.[4]

There are variations in structural attributes and extracellular matrix compositions along with tissue turnover. Interestingly, load-bearing tissues like tendons, ligaments, skin, muscles, bones, *etc.* are highly anisotropic in healthy situations.[5] Loss of tissue anisotropy with disease progression is mainly associated with changes in collagen alignment besides alteration in ECM

[a]*School of Medical Science and Technology, Indian Institute of Technology Kharagpur, Kharagpur, West Bengal 721302, India. E-mail: sdhara@smst.iitkgp.ac.in*
[b]*Department of Physics, Indian Institute of Engineering Science and Technology Shibpur, Howrah, West Bengal 711103, India*

composition.[6] Notably, anisotropic tissues exhibit significant piezoelectric behaviour under mechanical stimuli. The piezoelectric properties may be stalled due to the changes in the ECM microenvironment. In fact, load-bearing tissues under dynamic situations always flash piezoelectric signal transduction. Therefore, restoring tissue anisotropy is crucial to mitigate the challenges posed by synthetic or semi-synthetic templates mimicking native ECM attributes. Notably, bones and fish scales are composed of a highly anisotropic mineralized matrix with significant piezoelectric properties.[7,8] Piezoelectric materials are particularly promising as they generate electrical cues under mechanical stress.[9] Therefore, a promising approach could be integrating them with a demineralized matrix while maintaining native ECM anisotropy, which serves as a biologically active template enriched with type I collagen,[10,11] a key extracellular matrix component.[12]

PVDF, being a biocompatible, chemically resistant polymer with notable piezoelectric and ferroelectric properties, has gained attention for tissue engineering,[13] leading to a high β-phase content (>80%) and excellent piezoelectric performance.[14] In contrast, the existing poling technology requires a post-processing method[15] that aligns dipoles in pre-formed films using an electric field, often with heating or stretching. While it can convert the α-phase to β-phase below 70%, resulting in moderate piezoelectric enhancement. Finally, the limitation of mechanical stiffness and relatively low rigidity in load-bearing environments[16] could be addressed through composite materials by combining PVDF along with the demineralized bone matrix (DBM).[17] A recent study on energy harvesting application involves pulverization of fish scales into a powder form,[18] blending with PVDF in the solution phase, followed by chemical crosslinking. However, native ECM architecture and its favourable piezoelectric properties are ignored while fabricating the blend composite film, which necessitated poling after crosslinking to restore inferior piezoelectricity.

A sustainable and biologically inspired approach to develop a piezo-responsive template by combining electrospun β-phase PVDF nanofibers with a demineralized extracellular matrix derived from fish scales (D-FS) could be interesting. A delicate demineralization approach would offer to preserve intrinsic ECM anisotropy of the native tissue that could be attempted to distinguish by small-angle X-ray scattering analysis. Therefore, the study explores fabrication of a hybrid scaffold[19] by combining PVDF with a demineralized extracellular bone matrix sourced from fish scales. PVDF nanofibers were electrospun at varying w/v% *i.e.*, 10%, 12%, 15%, and 18%, over D-FS, forming layered biotemplates with tailorable electromechanical properties. Structural and functional evaluations *via* X-ray Diffraction (XRD) and Small-Angle X-ray Scattering (SAXS) confirmed enhanced crystallinity and alignment towards native anisotropy. Electrical analysis revealed effective piezoelectric behaviour under mechanical stimuli. Biological assessments showed strong cytocompatibility and tissue-regenerative potential, highlighting this platform as promising for skeletal tissue engineering without the need for secondary surgeries.

2. Materials and methods

2.1. Materials

Fish scales were collected from the local market in Kharagpur, India; chemicals used included hydrochloric acid (HCl, 37%, AR grade, Emplura, India), sodium sulfate (Na_2SO_4, anhydrous, ≥99%, Merck, India), polyvinylidene fluoride (PVDF; $M_W \approx 180\,000$ g mol^{-1}, HiMedia, India), *N*,*N*-dimethylformamide (DMF; anhydrous, ≥99%, Merck, India), and acetone (analytical reagent grade, ≥99.5%, Emplura, India).

2.2. Demineralization of the fish scale matrix

The complete protocol for the demineralization is illustrated in Fig. 1a, in which 20 g of raw fish scales, named Control Fish-Scale (C-FS), was utilised for preparation of the demineralized matrix. The raw scales were washed with distilled water frequently for 6 h, followed by 0.5 M HCl treatment for 6 h.[20] After treating with acid, the scales softened as the level of calcium was reduced. Then, the scales were neutralized using 5% sodium sulphate for 4 h. Followed by neutralization, the scales were kept at −20 °C refrigerator for structural stabilization followed by lyophilization. The Demineralized Fish Scale (D-FS) is shown in Fig. 1b.

2.3. Electrospinning of PVDF

Different concentrations of PVDF (10%, 12%, 15%, and 18% w/v) were prepared by dissolving PVDF in a DMF/acetone solvent mixture (2 : 1, v/v).[21] The mixture was kept under magnetic stirred for 2 h at 70 °C and 100 rpm (Fig. 1c). The optimization parameters for electrospinning of PVDF solution are provided in the SI (Table S1). The obtained homogeneous, transparent solutions was transfered into syring. The syringe containing PVDF solution was connected to the syringe pump. Electrospinning was performed at room temperature, and the optimization of the concentration of PVDF ink was done based on fiber morphology and phase analysis.[22]

2.4. Setup for alignment of PVDF nanofibers and electrospinning over D-FS

A setup was constructed using an arrangement of multiple thin spokes with a rotational speed of 1000 rpm and was grounded respect to high voltage, as mentioned in the patent application of our group. This arrangement enabled a high degree of fiber alignment in the nano range, which was evident through SEM imaging. Subsequently, D-FS were affixed to setup, and electrospinning was performed under similar condition while keeping the optimized nozzle to collector distance and the applied voltage. The electrospun PVDF over the demineralized fish scale is shown in Fig. 1d.

2.5. Physico-chemical characterization

2.5.1. Surface morphology analysis using SEM. The surface morphology of PVDF nanofibers of various concentrations was investigated by Field Emission Scanning Electron Microscopy (FESEM) (Gemini 300, ZEISS, Germany) analysis. The voltage

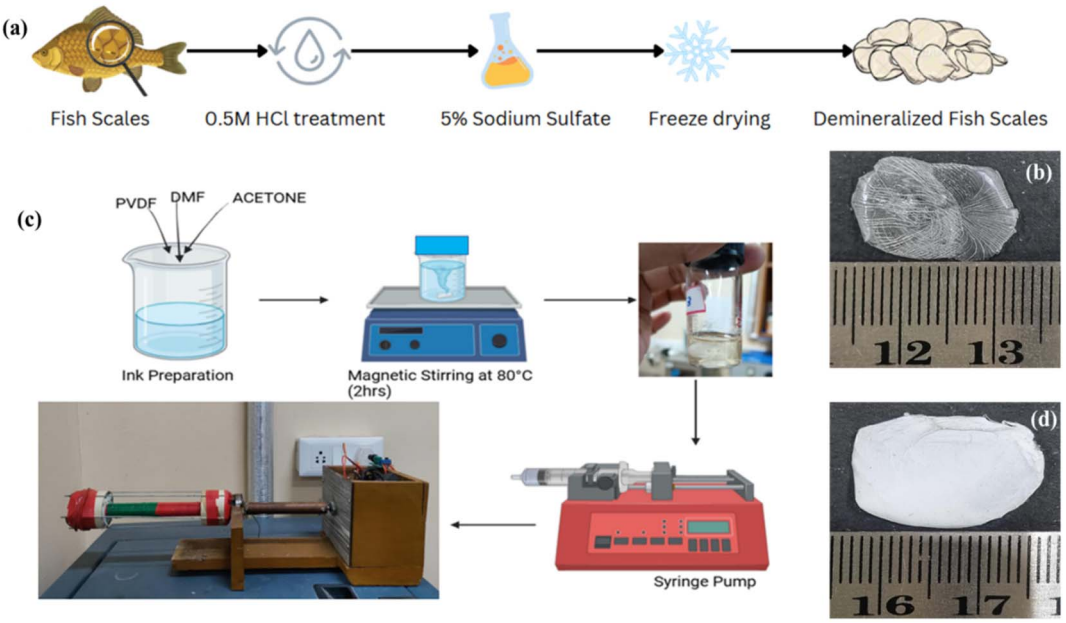

Fig. 1 (a and b) Flow diagram of methodology for demineralizing FS along with an optical image, named D-FS; (c and d) process for preparing PVDF ink over a non-conventional electrospinning setup and depositing over demineralized FS, named E-FS.

was set to 5 kV to obtain high-resolution images of PVDF nanofibers. The elemental composition was analysed using Energy Dispersive X-ray Spectroscopy (EDS). MATLAB was used to process the extracted SEM image for detecting and analysing the dominant orientation angle of fiber-like structures by converting image into grayscale value. Adaptive histogram equalization was used before detecting edges using the Canny method. The Hough Transform was applied to identify prominent lines at the edge in the detected image. By analysing these lines, the code calculated the angles and determined the dominant fiber orientation as the mean angle of detected lines. Finally, the detected lines were visualized, and the dominant angle was displayed, providing valuable insights into the structural alignment of fibers in the image (Fig. 2).

2.5.2. Elemental and functional group analysis using XPS and FTIR. X-ray Photoelectron Spectroscopy (XPS) was performed using a PHI 5000 VERSA PROBE III (ULVAC PHI, USA) to analyse the presence of key elements with chemical states for electrospun PVDF templates. The system utilized a monochromatic Al Kα X-ray source with a focused beam (ranging from <10 μm to 300 μm), enabling high-resolution surface analysis. Rapid X-ray induced Secondary Electron Imaging (SXI) was employed to enhance spatial resolution and surface characterization. This analysis provided critical insights into the materials' surface chemistry, confirming the presence of key functional groups and verifying structural modifications. The alpha to beta phase transition of PVDF was analysed using Fourier Transform Infrared (FTIR) spectroscopy (M/S Thermo Fisher Scientific Instruments, USA) within the frequency range of 400–1000 cm^{-1}. The β-phase fraction of sample was determined using absorbance data of FTIR measurements, following previously reported studies,[8] and calculated using eqn (1).

$$F(\beta) = \frac{A(\beta)}{1.26A(\alpha) + A(\beta)} \quad (1)$$

where $F(\beta)$ represents the β-phase content, and $A(\alpha)$ and $A(\beta)$ correspond to the absorption peaks of the α-phase and β-phase, respectively.

2.5.3. Phase and scattering pattern analysis using XRD and SAXS. X-ray diffraction (XRD) analysis of PVDF nanofibers, C-FS, D-FS, and electrospun-FS was performed. The samples were examined using a Cu Kα radiation source ($\lambda = 1.5406$ Å) at 40 kV and 30 mA. Data were collected over a 2θ range from 10° to 70° with a step size of 0.02° and a scan rate of 1° per minute. The diffraction patterns were collected to assess the crystalline percentage with the structures. Small-Angle X-ray Scattering (SAXS) (Xenocs S.A., France) is a powerful technique used for analysing the nanostructure properties of materials, particularly in biomaterials and polymer-based scaffold templates. The analysis provides essential information about the morphology, scattering patterns and crystalline phases of electrospun fibers, aiding in the assessment of their structural integrity and functional properties up to the depth of 0.5 μm from the sample surface.

2.5.4. Cyclic voltammetry (CV) for capacitive property measurement. Electrochemical behaviour was evaluated using Cyclic Voltammetry (CV). The sample were soaked in 6 M potassium hydroxide electrolyte for 30 minutes. Measurements were performed using copper electrodes connected to a potentiostat (BioLogic SP 150, France), and graphs were analysed using EC-Lab software.

2.5.5. Mechanical properties. A universal testing machine (H25KS, Hounsfield, UK) was used to measure uniaxial tensile strength (sample size: 10 mm × 15 mm × 0.2 mm) along the longitudinal axis. The test was conducted with a crosshead speed

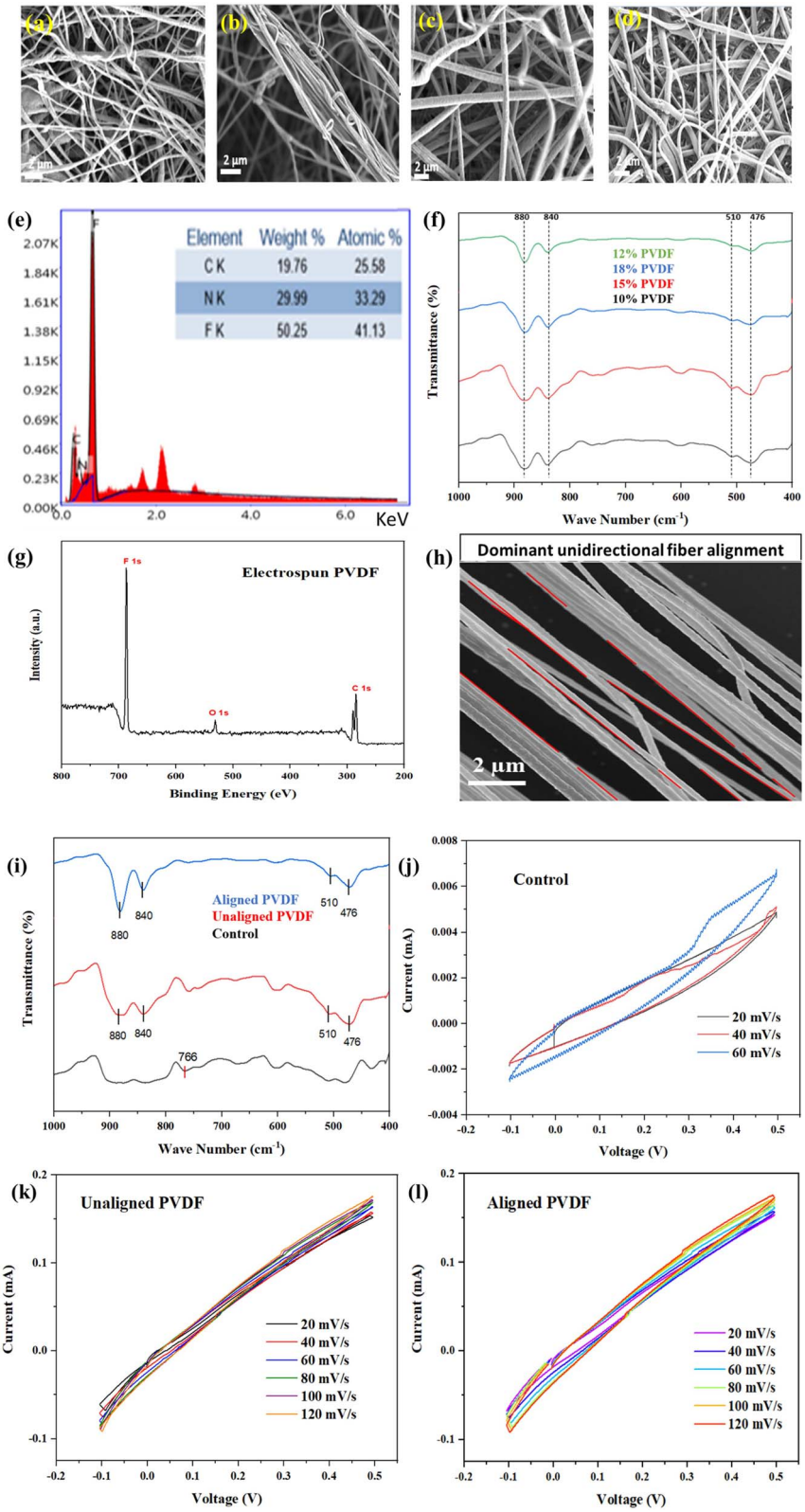

Fig. 2 (a–d) SEM images of 10%, 12%, 15%, and 18% PVDF nanofibers in w/v, with a scale bar of 2 μm; (e) EDX spectra of 12% PVDF nanofibers; (f) FTIR spectra of respective electrospun PVDF for confirming alpha to beta transition; (g) XPS spectrum of the electrospun PVDF sheet shows the existence of essential elemental constituents; (h) degree of alignment measured using SEM analysis for PVDF nanofibers (marked in red colours) using MATLAB, scale bar of 2 μm; comparison of (i) FTIR spectra for analysing vibration of bonds; (j–l) CV profiles for analysing the capacitive properties between control (α-PVDF), unaligned and aligned PVDF nanofibers.

of 0.5 mm min^{-1} and a maximum load cell capacity of 100 N. At least 5 measurements were carried out for testing each sample.

2.6. Piezo-characterization

2.6.1. Dielectric and conductivity measurements. Dielectric and conductivity measurements were measured using an impedance analyzer (HIOKI IM3570), which operates in a wide frequency range of 4 Hz to 5 MHz, and enables an impedance measurement precision of ±0.08% in case of LCR and continuous sweep modes. Its advanced signal processing allows for the assessment of dielectric constant, dielectric loss, and AC conductivity, making it suitable for analysing the frequency-dependent response of electroactive materials such as PVDF-based scaffold templates.

2.6.2. Voltage measurement. The piezoelectric voltage response was measured using a Keysight DSOZ1107A Digital Storage Oscilloscope, which offers a 1 GHz bandwidth and an 8 GSa/s maximum sampling rate for ensuring high-resolution signal acquisition. The oscilloscope offers a low noise floor and advanced waveform analysis capabilities to enable precise detection of voltage generated by piezoelectric response. The piezoelectricity performance of PVDF films was studied by finger tapping method with a force of 1.32 N. The resulting voltage were recorded in real time for evaluating its' energy-harvesting capability.

2.7. *In vitro* biological assessment

2.7.1. Protein adsorption. For the protein adsorption study, the samples were placed in a 24-well plate and incubated with 300 μL of a 0.1% bovine serum albumin (BSA, fraction V, Merck) solution prepared in phosphate-buffered saline (PBS, pH 7.4). Following incubation at 37 °C for 2, 4, 6, and 8 h, the samples were rinsed with PBS, and the adsorbed proteins were subsequently eluted using 300 μL of a 2% sodium dodecyl sulfate (SDS) solution made in PBS. The concentration of the adsorbed proteins was quantified using a bicinchoninic acid (BCA) assay kit (Sigma), which included BCA reagent and a 4% copper sulfate pentahydrate solution mixed in a 50 : 1 ratio, following the manufacturers' protocol. The absorbance of the resulting purple-blue protein complex was recorded at 562 nm using a microplate reader (Bio-Rad, iMark).

2.7.2. Hemocompatibility assay. The hemocompatibility assay was conducted to assess the interaction of C-FS and D-FS samples with red blood cells (RBCs) and evaluate their blood compatibility by obtaining necessary approvals from Datta Meghe Institute of Higher Education and Research, Wardha, after obtaining informed consent of the patient and with permission of the Institutional Ethics Committee (IEC Letter No.: DMIMS(DU)/IEC/MAY-2019/8731), following ASTM standard F756 (Standard Practice for Assessment of Hemolytic Properties of Materials). Materials were classified based on their hemolytic index values: below 2% are considered non-hemolytic, 2–5% slightly hemolytic, and above 5% hemolytic.[17] Blood was collected from a donor, and ethylenediaminetetraacetic acid (EDTA) was added to prevent coagulation. RBCs were isolated by centrifuging the blood at 4 °C for 10 minutes and washing the cells three times with PBS (pH 7.4). The assay was carried out to determine the extent of red blood cell lysis in the presence of test samples, along with both positive and negative controls. Each experiment was performed in triplicate ($n = 3$). After the incubation period, the samples were centrifuged again, and the optical density of the supernatant was measured at 540 nm to evaluate hemolysis. The percentage of hemolysis was calculated using eqn (2).

$$\text{Hemolysis ratio}(\%) = \frac{(\text{supension} - \text{negative control})}{(\text{positive control} - \text{negative control})} \times 100\% \quad (2)$$

2.8. Cellular assessment using the L929 cell line

2.8.1. Sample preparation. Cleaned and dried samples (C-FS and D-FS) were sterilized using ethanol followed by multiple PBS washes. The samples were then placed in a 24-well plate and incubated with complete DMEM low-glucose medium (Gibco, Life Technologies) at 37 °C for 24 hours. Subsequently, 5×10^4 cells were seeded into each well and cultured for 1 and 3 days, with the medium refreshed every 24 hours.

2.8.2. Live/Dead assay. Cell viability on the samples seeded with L929 cells, as per ISO 10993 standard, was evaluated using a LIVE/DEAD assay kit (Life Technologies), following the manufacturer' instructions. In brief, after 1 and 3 days of cell culture, the samples were incubated with a staining solution containing 2 μM calcein-AM and 4 μM ethidium homodimer at 25 °C for 60 minutes. Prior to imaging, the samples were thoroughly rinsed with PBS to eliminate any nonspecific staining. The stained samples were then examined using an inverted fluorescence microscope (AxioVision, Zeiss).

2.9. Interpolation and image segmentation

The provided MATLAB script performed image analysis to quantify and visualize the spatial overlap between cells and cracks from two aligned grayscale images, one from SEM and another from cell imaging. After pre-processing steps such as grayscale conversion, resizing, and normalization, the code applied adaptive thresholding to segment cell regions and cracks, followed by morphological filtering to remove small artefacts. The intersection of the two masks was computed to identify overlapping areas, and the percentage of cell area coinciding with cracks was calculated as a metric. Additionally, the script created a visual interpolation between the SEM and cell images using linear blending, facilitating qualitative assessment of alignment and overlap.

2.10. Statistical analysis

The statistical analysis had significant disparity between the experimental data with control groups by one-way analysis of variance (ANOVA) and *t*-test was followed using GraphPad Prism software (version 5.02). The significance level was determined as $p < 0.05$.

3. Results and discussion

3.1. Surface morphology analysis using SEM

The SEM analysis of PVDF at various w/v % concentrations *i.e.* 10%, 12%, 15%, and 18% in DMF and acetone solution revealed that 12% PVDF produced more uniform electrospun fibers with

no bead formation (Fig. 2a and d). Elemental analysis of precursor elements present in 12% PVDF nanofibers under areal scanning with EDX is shown in Fig. 2e. Furthermore, 12% PVDF solution was electrospun using a rotating collector to produce uniformly aligned and smooth nanofibers with an average diameter of 100–250 nm,[23] as observed in the SEM image. MATLAB analysis of the corresponding micrograph confirmed a predominant unidirectional fiber orientation, with an average alignment angle of 44.46° (Fig. 2h). The output file generated from MATLAB detected the lines along the alignment, marked in red.

3.2. Elemental and functional group analysis

The FTIR spectra of various electrospun PVDF (Fig. 2i) exhibited distinct transmittance peaks at certain wavenumbers, signifying the presence of identifiable chemical linkages. The peaks at 840 cm^{-1} and 880 cm^{-1} indicate the β-phase of PVDF nanofibers, along with the peak at 880 cm^{-1} represents the CF_2 bending and secondary vibrations, whereas the peak at 840 cm^{-1} represents the CF_2 stretching and CH_2 bending, advantageous for piezoelectric applications.[24] The peaks at 510 cm^{-1} and 476 cm^{-1} affirm the polymer structure due to CF_2 bending and skeletal vibrations.[25] The β fraction values calculated using eqn (1) for 10%, 12%, 15%, and 18% PVDF were 54.4%, 67.0%, 59.5%, and 57.3%, respectively. Therefore, 12% PVDF has the most distinct peaks towards enhanced beta phase relative to different concentrations of PVDF nanofibers. Therefore, 12% PVDF offers an ideal composition, attaining a robust FTIR response, rendering it to improve piezoelectric characteristics towards intended application. The FTIR spectra of aligned 12% PVDF, unaligned 12% PVDF, and α-phase PVDF as control are presented in Fig. 2f. The peaks at 880 cm^{-1} and 840 cm^{-1}, associated with the β-phase are more prominent in aligned PVDF with respect to the unaligned sample. The control sample has a peak at 766 cm^{-1}, indicating the α-phase, which implies diminished piezoelectric performance.[26] The pronounced β-phase peaks in aligned PVDF indicate that fiber alignment facilitates phase transformation, resulting in enhanced piezoelectric characteristics. This investigation evidences that 12% PVDF, when aligned, demonstrates enhanced structural properties relative to its unaligned counterpart and the control sample.

The XPS analysis of electrospun PVDF evidences the existence of essential elemental constituents, as depicted in Fig. 2g, thereby validating its chemical composition. The spectrum displays significant peaks for fluorine (F 1s) at approximately 688 eV, carbon (C 1s) at around 285 eV, and oxygen (O 1s) at approximately 532 eV.[27] The prominent F 1s peak signifies a substantial presence of fluorine, a defining ingredient in PVDF, whereas the C 1s peak denotes the polymer backbone. The small O 1s peak indicates possible surface oxidation or environmental contamination, as the experiment was performed in an open atmosphere. These results validate the effective production of electrospun PVDF fibers exhibiting anticipated chemical characteristics required for their piezoelectric nature.

3.3. CV profile of PVDF

Cyclic voltammetry (CV) curves (Fig. 2j–l) for control, unaligned, and aligned PVDF samples were recorded within a potential range of −0.1 V to 0.5 V to examine their electrochemical behaviour.[28] The control sample demonstrates reduced current responses, signifying restricted charge storage capacity. The unaligned PVDF exhibits an augmented current response with a nearly symmetrical profile at various scan rates (20–120 mV s^{-1}), indicating enhanced charge transport characteristics. The aligned PVDF further amplifies this tendency, exhibiting an elevated current response and distinct capacitive behaviour, due to enhanced molecular alignment and better charge conduction pathways. The observed variations in CV characteristics indicate that molecular orientation significantly influences the electrochemical performance of PVDF, with aligned PVDF demonstrating enhanced charge storage capacity, rendering it a viable choice for energy storage and sensing applications.

3.4. Phase and scattering pattern analysis using XRD and SAXS

The XRD patterns of control or PVDF in the α phase, unaligned and aligned PVDF samples exhibit unique structural features affected by molecular orientation, as depicted in Fig. 3a–c. Control sample exhibits a significant peak at 19.9°, indicative of the α-phase, with a crystallinity of 70.08%, signifying a highly organized structure. The unaligned PVDF sample exhibits a peak shift to 20.23° and a diminished crystallinity of 54.62%, indicating an elevated amorphous content resulting from the disordered polymer chain configuration. The aligned PVDF sample exhibits a shift to 20.28° and an intermediate crystallinity of 61.95%, indicating enhanced chain orientation with a partial transition to the β-phase.[29] The enhancement in crystallinity from unaligned to aligned underscores the significance of molecular alignment in improving crystalline order, which is essential for optimising mechanical and piezoelectric capabilities in PVDF-based applications.

The SAXS analysis of control, unaligned PVDF, and aligned PVDF samples elucidates their structural organization and changes in crystallinity, as depicted in Fig. 3d–f. The scattering intensity curves reveal that the control sample demonstrates a pronounced drop, indicating a more compact and less ordered structure with increased crystallinity. The unaligned PVDF sample exhibits a more gradual decline in intensity, indicating a decrease in crystallinity resulting from the random orientation of polymer chains. The oriented PVDF exhibits an intermediate trend, indicating a partial augmentation of crystallinity due to orientation. Furthermore, the combined scattering intensity curve and the corresponding 2D SAXS patterns show distinct variations in color intensity distribution based on the degree of structural ordering and orientation within the samples, as presented in the SI (Fig. S2).[30]

The control sample demonstrates a more isotropic scattering pattern, signifying homogeneous nanostructures. The unaligned PVDF sample exhibits a wider, diffuse scattering pattern with reduced intensity, indicating a decrease in structural order. Concurrently, the oriented PVDF exhibits an anisotropic

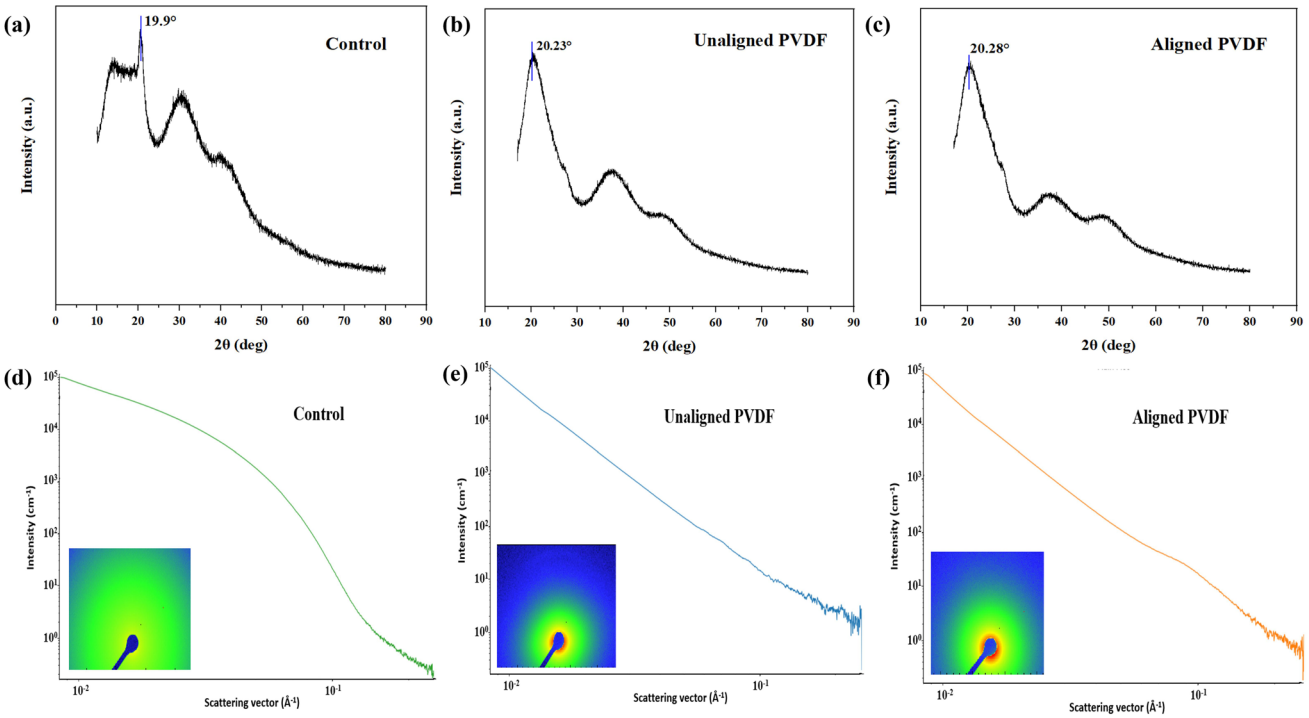

Fig. 3 Comparison of (a–c) XRD spectra for evaluating the crystallinity percentage; (d–f) scattering pattern and plot using SAXS analysis between control (α-PVDF), unaligned, and aligned PVDF nanofibers.

scattering pattern characterized by increased spots, hence affirming improved molecular alignment. The findings underscore the impact of molecular arrangement on the crystalline structure of PVDF, with alignment promoting enhanced order and crystallinity relative to unaligned configurations.

3.5. Dielectric and conductivity measurements

The dielectric characteristics of control, unaligned, and aligned PVDF samples were examined by frequency-dependent dielectric constant, dielectric loss, and AC conductivity tests, as seen in

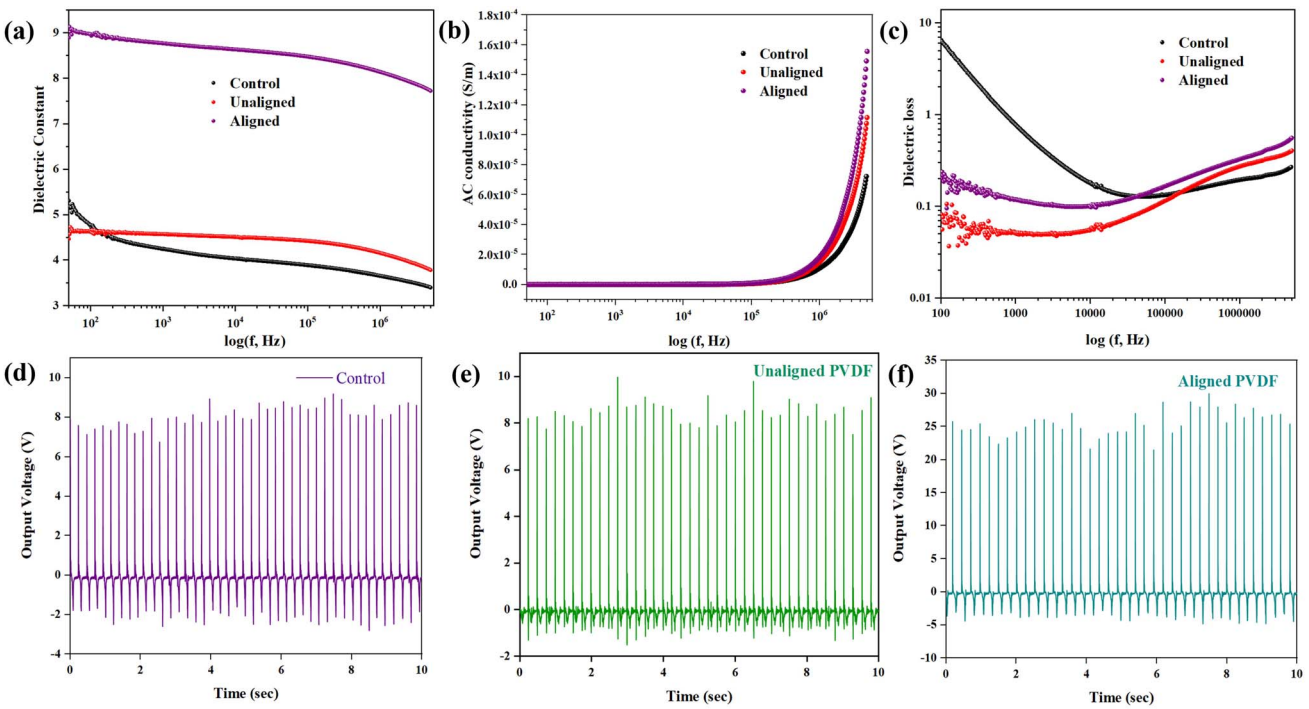

Fig. 4 Comparison of (a–c) dielectric constant, AC conductivity and dielectric loss, respectively; (d–f) comparison of voltage output upon finger tapping between control, unaligned and aligned PVDF nanofibers, respectively, as obtained using a digital oscilloscope.

Fig. 4a–c. The dielectric constant graph indicates that the aligned PVDF sample demonstrates superior values throughout the frequency spectrum, signifying improved polarisation and dipole alignment relative to the control and unaligned PVDF. The highest dielectric constant is attained in aligned PVDF, which is 1.8-fold more than that of the control.[31] The dielectric loss curves exhibit a declining trend with increasing frequency, with the aligned PVDF showing comparatively lower losses at elevated frequencies, indicating diminished energy dissipation and enhanced stability. The conductivity of PVDF exhibits an exponential increase with alignment, achieving a maximum value of 1.6×10^{-4} S m^{-1} for aligned PVDF, which exceeds the Control conductivity of 8×10^{-5} S m^{-1}. This enhancement in conductivity for the aligned PVDF sample is likely attributable to improved charge transport pathways resulting from molecular alignment.

3.6. Voltage measurement

The voltage output plots derived from a digital oscilloscope demonstrate piezoelectric response of PVDF nanofiber sheets (1.5 cm × 1.5 cm) when subjected to finger tapping.[32] Fig. 4d–f illustrate the Control sample, wherein PVDF is in its α-phase, demonstrating the lowest voltage output attributable to its limited piezoelectric activity. unaligned PVDF exhibits a significant rise in output voltage relative to the control, indicating improved piezoelectric properties attributed to partial β-phase development. The aligned PVDF produced the highest voltage output, approximately 30 V, signifying a notable enhancement in piezoelectric performance. This improvement is due to increased alignment, which encourages β-phase crystallization and aids dipole orientation, resulting in enhanced charge production under mechanical stress.

3.7. Analysis of surface morphology of D-FS using SEM

The SEM images and EDX spectra of the pristine fish scale (C-FS) and Demineralized Fish Scale (D-FS) samples highlight significant structural and compositional variations. The SEM image of C-FS (Fig. 5a) displays a dense, mineral-rich surface, whereas that of D-FS (Fig. 5b) reveals a more porous, fibrous morphology attributed to the removal of apatite crystals. EDX analysis of C-FS confirms high levels of calcium (Ca) and phosphorus (P), indicative of the hydroxyapatite phase, along with trace amounts of magnesium (Mg) and sodium (Na). In contrast, the EDX spectrum of D-FS shows a notable reduction in Ca and P signals, coupled with an increase in carbon (C) and oxygen (O), reflecting a shift toward an organic-dominated composition after demineralization. Structural characterization further identifies that the typical *d*-spacing of collagen fibrils is around 67 nm, consistent with type I collagen, confirming that the collagen matrix remains intact.[33] These results collectively demonstrate the effective removal of mineral content while preserving the hierarchical structure of collagen in the D-FS.

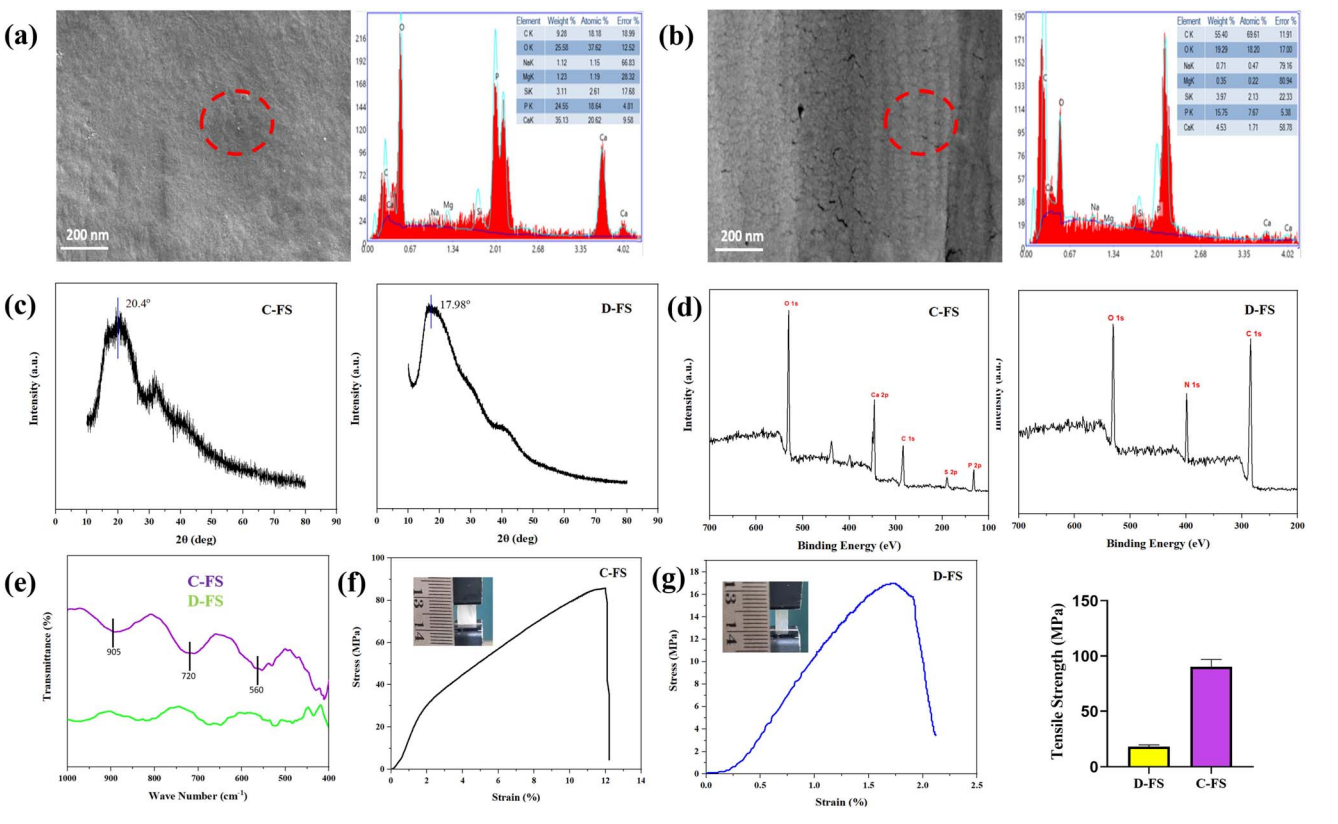

Fig. 5 (a) SEM and EDX analysis of C-FS, with a scale bar of 200 nm; (b) SEM and EDX analysis of D-FS, with a scale bar of 2 μm; (c) XRD spectra for analysis of crystallinity percentage of C-FS and D-FS; comparison of (d) XPS spectra for elemental analysis; (e) FTIR spectra; (f) decrease in tensile strength due to demineralization of C-FS; (g) stress–strain graphs of C-FS and D-FS.

3.8. Physical characterisation of demineralized fish scales (D-FS)

The XRD patterns of C-FS and D-FS reveal clear differences in crystallinity and structural composition (Fig. 5c). C-FS exhibits a sharp diffraction peak at $2\theta = 20.4°$, characteristic of the well-organized collagen structure, along with additional crystalline signals associated with hydroxyapatite. In contrast, D-FS presents a broad peak centered at $2\theta = 17.98°$, indicative of a predominantly amorphous structure due to the removal of mineral content.[34] This structural transformation is further supported by crystallinity index analysis, which shows a high crystallinity of 67.76% in C-FS for the presence of minerals, while D-FS demonstrates a markedly lower crystallinity of 9.40%, highlighting the effective removal of the mineral phase and the preservation of a large amorphous collagen framework. XPS spectra illustrated in Fig. 5d for C-FS and D-FS have unique elemental compositions, indicating the elimination of the mineral phase during demineralization. The C-FS spectrum reveals significant peaks for oxygen (O 1s), calcium (Ca 2p), phosphorus (P 2p), and carbon (C 1s), signifying the existence of hydroxyapatite in conjunction with the organic collagen matrix. Conversely, the D-FS spectrum does not exhibit distinct Ca 2p and P 2p peaks, affirming the successful elimination of the mineral phase. The D-FS exhibits a prominent C 1s peak, accompanied by O 1s and an extra nitrogen (N 1s) peak, which is ascribed to the presence of collagen proteins. The findings indicate a shift from a mineralized composite structure in C-FS to a collagen-dominant organic matrix in D-FS, consistent with the structural and compositional changes caused by the demineralization process.[35]

The FTIR spectrum (Fig. 5e) of C-FS reveals distinctive peaks associated with vibrational modes of phosphate (PO_4^{3-}) in calcium-based apatite crystals, occurring within the range of 900–400 cm^{-1}. The notable peak at approximately 560 cm^{-1} is ascribed to bending vibrations of phosphate groups, whereas the peak near 900 cm^{-1} is associated with stretching vibrations of PO_4^{3-}. The peak at approximately 720 cm^{-1} corresponds to the carbonate (CO_3^{2-}) group. The D-FS spectrum lacks these peaks, as heavy minerals were eliminated during the demineralization process. This resulted in the retention of the organic matrix, predominantly consisting of collagen, which does not exhibit phosphate- and carbonate-related vibrational bands.[36]

3.9. Mechanical performance of demineralized fish scales (D-FS)

The tensile stress–strain curves of C-FS and D-FS reveal substantial disparities in mechanical properties, indicating the influence of demineralization on structural integrity. The C-FS has a maximum stress of 85.7 MPa, owing to reinforcement from the hydroxyapatite mineral phase, which enhances the fish scale stiffness and load-bearing capacity, as depicted in Fig. 5f. Conversely, D-FS has a markedly diminished maximum stress of 17 MPa, signifying a substantial reduction in mechanical strength attributable to elimination of the mineral phase, resulting in a soft, collagen-dominant matrix. The strain at failure is significantly greater in C-FS, underscoring the composite characteristics of the mineralized fish scale, which equilibrates stiffness and toughness,[37] as depicted in Fig. 5g. The decline in mechanical characteristics during demineralization underscores the essential function of hydroxyapatite in augmenting the structural integrity of fish scales, and retained collagen matrix in D-FS maintains a degree of flexibility.

3.10. *In vitro* bioassay of D-FS

The hemolysis analysis (Fig. 6a) reveals a significantly higher hemolytic activity in C-FS, indicating cytotoxicity, while the D-FS exhibits minimal hemolysis, falling within the non-hemolytic range. The visual observations of supernatants confirm these results, with the D-FS displaying a lighter coloration compared to the deep red of C-FS and the positive control water, suggesting reduced red blood cell (RBC) lysis. SEM images (Fig. 6b) of the D-FS surface show well-preserved RBC morphology, with smooth, round cells and minimal membrane disruption (marked in yellow), further confirming its hemocompatibility. Overall, the D-FS demonstrates favourable blood compatibility.

The graph (Fig. 6e) illustrates the protein adsorption capacity of D-FS and E-FS over different incubation periods (2, 4, 6, and 8 hours). Both D-FS and E-FS exhibit a time-dependent increase in protein adsorption, indicating improved surface interaction over extended durations. D-FS shows a statistically significant increase in adsorption between each time interval, with the highest protein adsorption ($\sim$400 μg mL^{-1}) observed at 8 hours (**p <0.01; ***p <0.001). E-FS also demonstrates enhanced adsorption with time. At 8 hours, E-FS achieves a slightly higher protein adsorption than D-FS, suggesting superior performance in prolonged interactions with proteins. Further degradation and swelling studies of C-FS, D-FS, and E-FS were systematically evaluated to understand the effects of demineralization and integration of electrospun PVDF over D-FS based on hydrophilicity and structural stability, as presented in the SI (Fig. S1). Overall, these results indicate that the material effectively supports protein adsorption, with controlled swelling and degradation in a biological environment.

The MTT assay results (Fig. 6f) indicate a significant difference in cell viability between C-FS and D-FS on both 1 and 3 days post-seeding.[38] On day 1, D-FS exhibits markedly higher cell viability compared to C-FS, suggesting a more favourable microenvironment for initial cell attachment and proliferation. On day 3, this disparity becomes even more pronounced, with D-FS supporting robust cell growth, while C-FS maintains low viability. The statistically significant differences (***p <0.001) at both time points highlight the cytotoxic nature of C-FS, likely due to residual impurities or poor cytocompatibility. In contrast, D-FS demonstrates excellent cytocompatibility, supporting sustained cellular proliferation and indicating its potential for use in tissue engineering applications. Cell viability on C-FS and D-FS samples was evaluated using LIVE/DEAD staining, and representative fluorescence images are shown in Fig. 6c and d. The images captured on day 3 clearly demonstrate a high proportion of viable cells on the D-FS surface, confirming its excellent cytocompatibility. SEM imaging further supports this observation by showing that cells preferentially adhered to the demineralized regions of the D-FS scaffold template, indicating a favourable microenvironment for cell attachment. In contrast, the C-FS sample exhibited

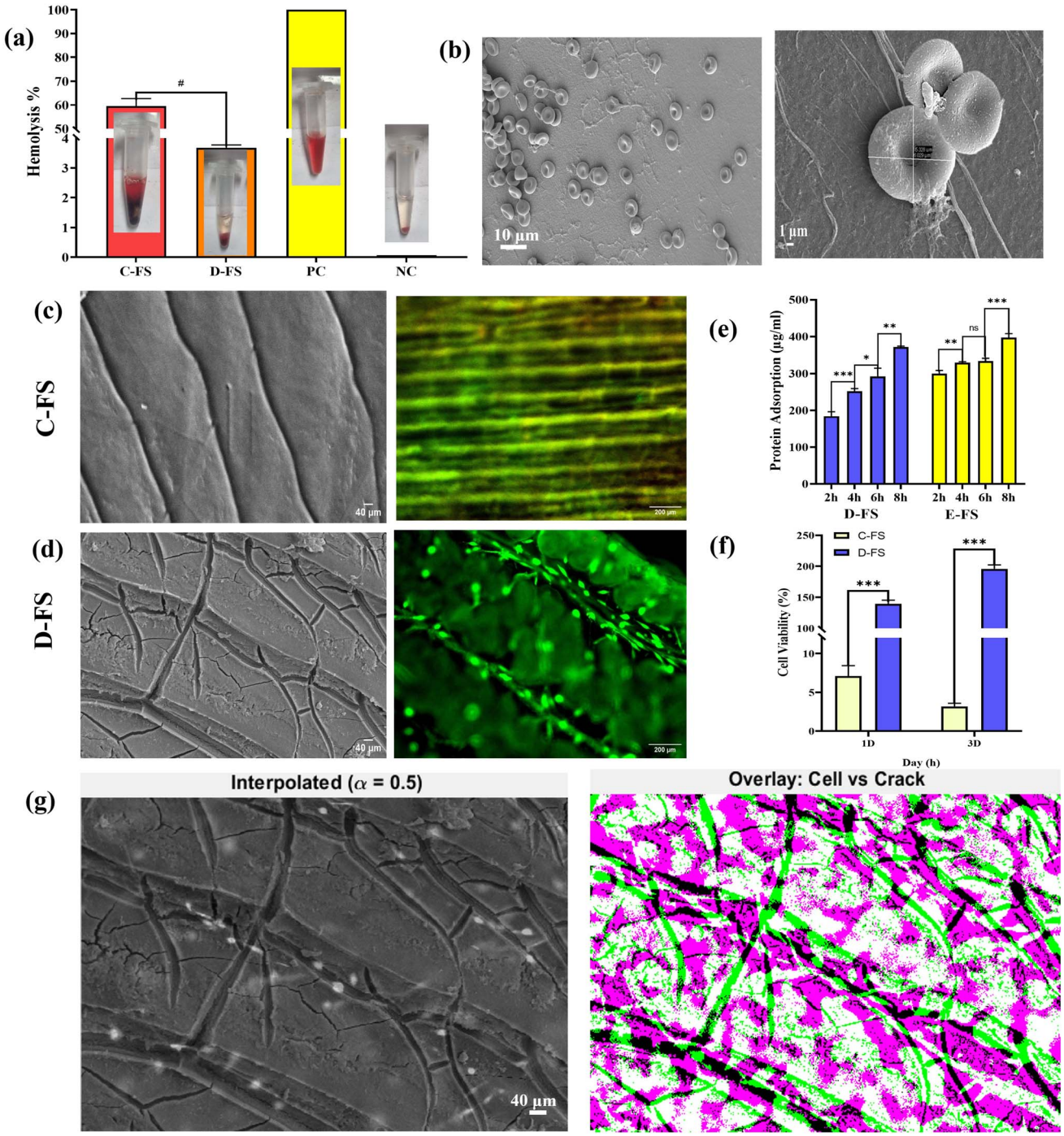

Fig. 6 *In vitro* studies: (a and b) hemocompatibility evaluation to assess the extent of hemolysis and SEM analysis of RBC morphology in D-FS; (c) SEM image of C-FS along with LIVE/DEAD staining of C-FS on day 3; (d) SEM image of D-FS and LIVE/DEAD staining on day 3 showing cell adhesion on demineralized regions; (e) protein adsorption analysis of D-FS and E-FS; (f) MTT analysis showing the difference in cell viability between C-FS and D-FS; (g) interpolated image blends both modalities ($\alpha = 0.5$) to aid visual interpretation, and the binary overlay highlights co-localization of cells (violet) with cracks (green), revealing that 74.03% of cell area overlaps demineralized regions.

predominantly dead cells, likely due to the cytotoxic effects of residual heavy metals.

Evaluating the cellular adhesion in relation to surface demineralization, we analysed the interaction between L929 fibroblast cells and a demineralized fish scale substrate using image-based quantification techniques (Fig. 6g). High-resolution SEM images (1024 × 696 pixels) were obtained from D-FS, where surface cracks (marked in red) visually represent the demineralized regions. These were in line with fluorescence microscopy images showing the presence of L929 cells (marked in yellow) on the D-FS substrate. Following grayscale normalization, alpha blending ($\alpha = 0.5$) was employed to

produce a composite visualization, enabling qualitative assessment of cellular alignment with surface features. Subsequently, adaptive thresholding and morphological filtering were applied to generate binary masks for both the cell-covered areas and the crack regions. Overlap analysis revealed that 74.03% of the total cell area was localized on the cracked (demineralized) regions of the substrate. This significant overlap suggests that L929 cells exhibit preferential adhesion to demineralized zones of the fish scale, a behaviour not observed on control (non-demineralized) surfaces. This method provides both visual and quantitative confirmation that surface demineralization enhances cellular attachment, highlighting its potential role in designing bioactive substrates for tissue engineering applications.

3.11. Surface morphology of electrospun PVDF over D-FS

The SEM image of E-FS (Fig. 7a) shows a bilayered piezo template for demonstrating the effective incorporation of polymeric nanofibers over D-FS. The yellow color areas represent the electrospun PVDF nanofibers, characterized by a consistent and aligned structure, whilst the red-highlighted areas denote the exposed surface of the fish scale (FS). The PVDF nanofibers add a supplementary structural layer, improving the composite mechanical flexibility and potential piezoelectric characteristics, while the underlying fish scale serves as a natural collagen-based scaffold template.[39]

The FTIR spectra of D-FS and electrospun PVDF over D-FS (E-FS) exhibit unique structural features according to their compositions (Fig. 7b). The D-FS spectrum has a wide transmittance profile, predominantly indicative of the collagen-rich matrix, devoid of identifiable crystalline characteristics. Conversely, E-FS spectrum exhibits distinct absorption peaks at 840 cm^{-1} and 880 cm^{-1}, indicative of the β-phase of PVDF,[40] hence confirming the effective integration of electrospun polymer onto the demineralized fish scale surface. The existence of these peaks indicates an improvement in structural order and crystallinity attributed to the PVDF coating. The spectral distinctions between D-FS and E-FS highlight the transition from an entirely organic collagen scaffold to a composite system with enhanced mechanical and electrical properties.

The XRD patterns of D-FS (Fig. 5c) and E-FS show structural alteration due to electrospinning (Fig. 7c). The D-FS displays a wide diffraction peak at $2\theta = 17.98°$, signifying an amorphous collagen matrix with low crystallinity, measured at 9.40%. Conversely, the E-FS shows peak at $2\theta = 20.5°$, indicative of β-phase crystalline structure in alinged PVDF, accompanied by a markedly enhanced crystallinity of 40.30%.[41] This improved crystallinity indicates the effective integration of the electrospun PVDF onto the fish scale matrix by enhancing structural organization and enhanced mechanical and functional capabilities, including the piezoelectric action.[42]

3.12. Phase and scattering pattern analysis of E-FS

The SAXS study of D-FS (Fig. 5d) and E-FS demonstrates notable disparities in their nanoscale structural organization (Fig. 7d).[43] The scattering pattern of D-FS displays a diffuse and indistinct ring structure, signifying a generally disordered configuration with limited crystalline organization, typical of the collagenous matrix post-demineralization. Conversely, the scattering pattern of E-FS exhibits more pronounced and clearly defined concentric rings, indicating an enhancement in nanoscale order and structural alignment. The augmented scattering response in E-FS is ascribed to the incorporation of electrospun PVDF nanofibers, which promote crystallinity and molecular orientation in the composite. The shift from a disorganized collagen matrix in D-FS to a more organized structure in E-FS underscores strengthening influence of PVDF integration.

The XPS spectra of D-FS and E-FS exhibit unique surface chemical compositions (Fig. 7e). Both spectra have significant peaks for O 1s, C 1s, and N 1s, signifying the existence of functional groups comprising oxygen, carbon, and nitrogen.[44] The relative strength of the C 1s peak in E-FS is significantly greater than that of the peak in D-FS, attributable to the inclusion of PVDF nanofibers, predominantly consisting of carbon-based polymer chains. The diminished N 1s intensity in E-FS indicates a potential surface covering effect resulting from PVDF deposition, which may obscure some nitrogen-containing functions within the underlying fish scale matrix. The differences in surface chemistry suggest the successful integration of PVDF onto the fish scale, potentially increasing its physicochemical properties.

3.13. Tensile strength analysis of E-FS

The UTM stress–strain curves of D-FS (Fig. 5g) and E-FS demonstrate a notable improvement in mechanical properties following the addition of PVDF, as shown in the stress–strain curve (Fig. 7f). D-FS exhibits a maximum stress of 17 MPa with constrained strain capacity, signifying diminished mechanical strength attributable to the lack of the mineral phase. Conversely, E-FS attains a significantly elevated tensile strength of 49.6 MPa, coupled with an enhanced strain-to-failure, underscoring the reinforcing impact of the electrospun PVDF layer (Fig. 7g). This improvement is due to the enhanced mechanical properties of PVDF,[45] which confer structural integrity and load-bearing capability to the composite material. The findings validate the effective alteration of fish scale-derived biomaterials *via* electrospinning.

3.14. Dielectric and conductivity measurements

Dielectric studies of D-FS and E-FS demonstrate substantial improvements in dielectric characteristics following the addition of PVDF (Fig. 8a and b). The dielectric loss curves demonstrate a declining trend with increasing frequency for both samples, with E-FS displaying marginally larger losses, indicating enhanced charge storage capacity. The AC conductivity of E-FS is significantly improved at elevated frequencies, indicating enhanced charge transfer, presumably due to the superior conductivity and reduced interfacial polarisation conferred by PVDF. The findings indicate that the electrospun PVDF layer markedly enhances the dielectric and electrical characteristics of the fish scale material.[46] The voltage output analysis from finger tapping, conducted with a digital oscilloscope, demonstrates

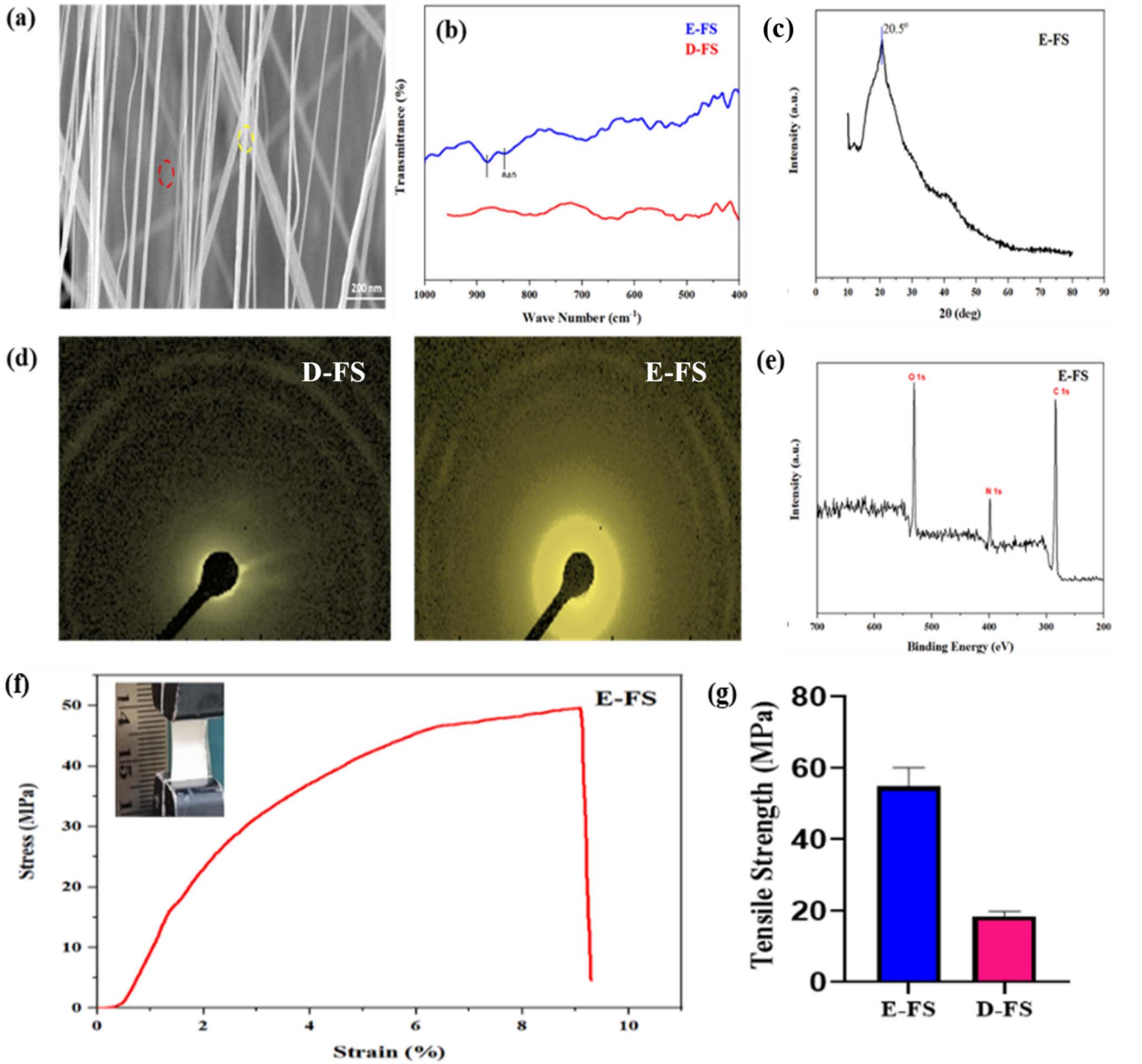

Fig. 7 (a) SEM image of E-FS where yellow and red markings denote PVDF nanofibers and the FS surface, respectively, with a scale bar of 200 nm; comparison of (b) FTIR spectra between D-FS and E-FS; (c) XRD spectrum of E-FS; (d) SAXS analysis of isotropic and anisotropic scattering patterns of E-FS and D-FS; (e) XPS spectrum of E-FS; (f and g) stress–strain curve of E-FS, along with an increase in tensile strength of E-FS due to deposition of PVDF over D-FS.

a significant enhancement in the energy harvesting efficiency of E-FS relative to D-FS (Fig. 8c and d).

The D-FS sample demonstrates a diminished output voltage, with peaks nearing 0.75 V, signifying a feeble piezoelectric response. Conversely, the E-FS sample produces markedly elevated voltage peaks, with levels of up to 15 V, indicating a substantial improvement in piezoelectric efficacy. The enhancement is ascribed to the use of PVDF, recognized for its robust piezoelectric characteristics, and its efficient interaction with the demineralized fish scale matrix, resulting in improved dipole alignment under mechanical stimuli. The enhanced voltage output of E-FS indicates its prospective use in self-powered wearable sensors and energy harvesting systems.[18]

3.15. CV profiles of D-FS and E-FS

The CV profiles of D-FS and E-FS, recorded at scan rates of 20 mV s^{-1} and 120 mV s^{-1} (Fig. 8e and f), illustrate the electrochemical behaviour and capacitive characteristics of both the samples.[47] An increase in current was observed with increasing scan rate, accompanied by an enhanced capacitive response and faster charge/discharge kinetics. In the case of D-FS, the area enclosed by the CV curve at 20 mV s^{-1} is 0.023, which increases to 0.036 at

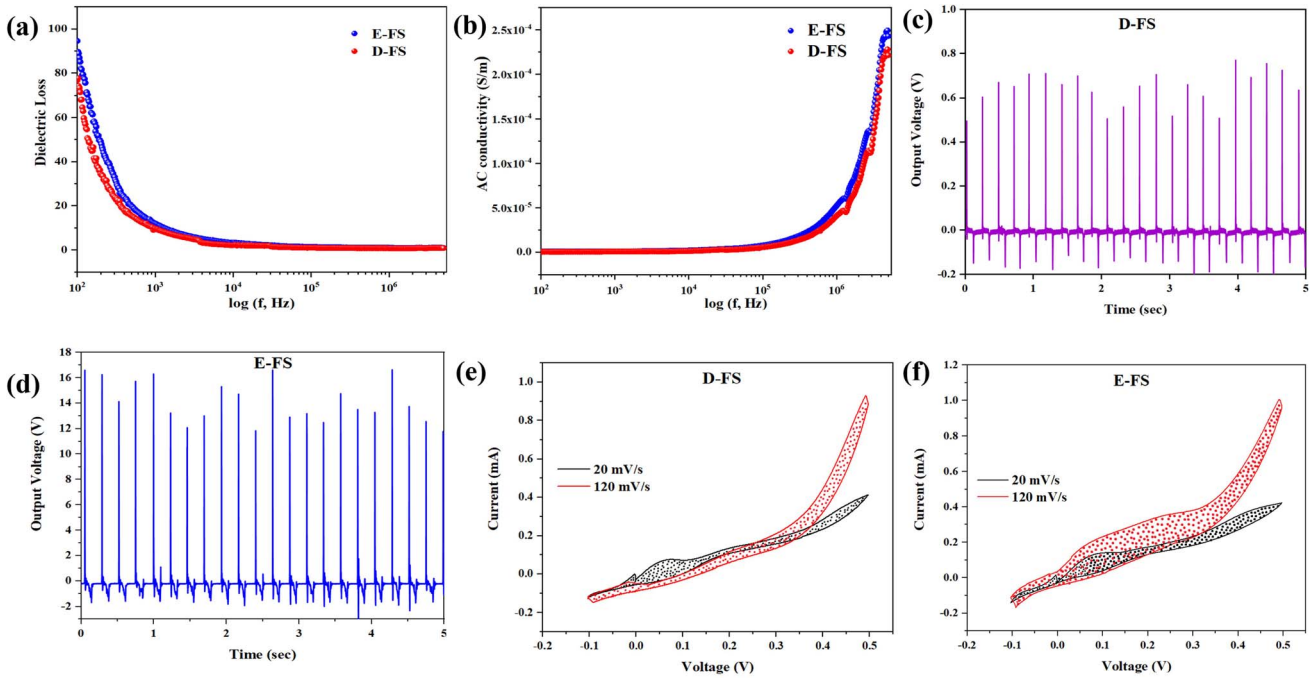

Fig. 8 Comparison of (a and b) dielectric loss and AC conductivity; (c and d) voltage output upon finger tapping using a digital oscilloscope; (e and f) CV curves for analysing capacitive properties between D-FS and E-FS.

120 mV s^{-1}—an enhancement of approximately 37%. In contrast, E-FS shows a significantly larger CV curve area of 0.032 sq. unit at 20 mV s^{-1}, which rises sharply to 0.085 sq. unit at 120 mV s^{-1}, with an increase in percentage of 62.1%. This substantial improvement highlights the contribution of the electrospun PVDF layer to enhancing the capacitive performance, likely due to better electrolyte accessibility, increased surface area, and improved dielectric properties imparted by the PVDF coating. Thus, the significantly larger area in E-FS compared to D-FS underscores the superior capacitive performance of the PVDF-modified structure. Moreover, the increase in current values with increasing scan rate for both D-FS and E-FS further confirms enhanced capacitive behaviour.

A comparative evaluation of the current–voltage (*I–V*) behaviour between the E-FS developed in this study and the PVDF/$BaTiO_3$/NiO composite underscores the effectiveness of E-FS in delivering mechano-electrical cues for cell differentiation and tissue regeneration. The CV analysis of E-FS reveals an increase in the enclosed area from 0.032 to 0.085 sq. unit with varying scan rates, indicating that transient charge transfer is an essential feature for stimulating biological responses without prolonged energy retention. In contrast, the PVDF/$BaTiO_3$/NiO composite exhibits a narrower current range, from 0.02 to 0.03 mA, and a broader quasi-rectangular CV profile characteristic of supercapacitors with high charge storage capacity. Such behaviour, while suitable for energy devices, is suboptimal for biomedical scaffolds where localized electrical impulses are required to modulate cell behaviour without long-term charge buildup. Thus, the E-FS demonstrates a high impulse current and rapid discharge capacity, making it well-suited for providing bioelectric stimuli that direct stem cell differentiation in regenerative medicine applications.

3.16. CV profile and piezoelectric measurement of multi-layered E-FS

The CV curves of multilayer E-FS recorded at two different scan rates, 20 mV s^{-1} and 120 mV s^{-1}, demonstrate a clear increase in both current response and the enclosed area with increasing scan rate (Fig. 9e), indicative of enhanced capacitive behaviour. At 20 mV s^{-1}, the area enclosed within the CV curve is 0.026, while at 120 mV s^{-1}, it increases substantially to 0.076, corresponding to an enhancement of approximately 65.9%. Furthermore, the increase in current response with the increase in scan rate reflects the material's ability to support faster ion transport and surface redox reactions.

The dielectric study of multilayer E-FS demonstrates a high dielectric constant at low frequencies (Fig. 9a and b), which progressively diminishes with increasing frequency, signifying pronounced interfacial polarization. The AC conductivity graph (Fig. 9c) displays a low conductivity plateau at lower frequencies, succeeded by a fast increase at higher frequencies, consistent with the hopping conduction mechanism in polymer-based composite materials.

The voltage output of the multilayer E-FS sample during periodic finger tapping, as measured with a digital oscilloscope (Fig. 9d), displays a sequence of acute voltage spikes with amplitudes nearing 25 V. The elevated output voltage indicates superior piezoelectric performance attributed to the layered construction, which presumably enhances charge accumulation and energy conversion efficiency. The uniformity of the peaks signifies consistent reaction behaviour, but the baseline variations imply slight mechanical instabilities or changes in the applied force. The observed output demonstrates capability of multilayer E-FS structures for application in self-powered sensing, where mechanical

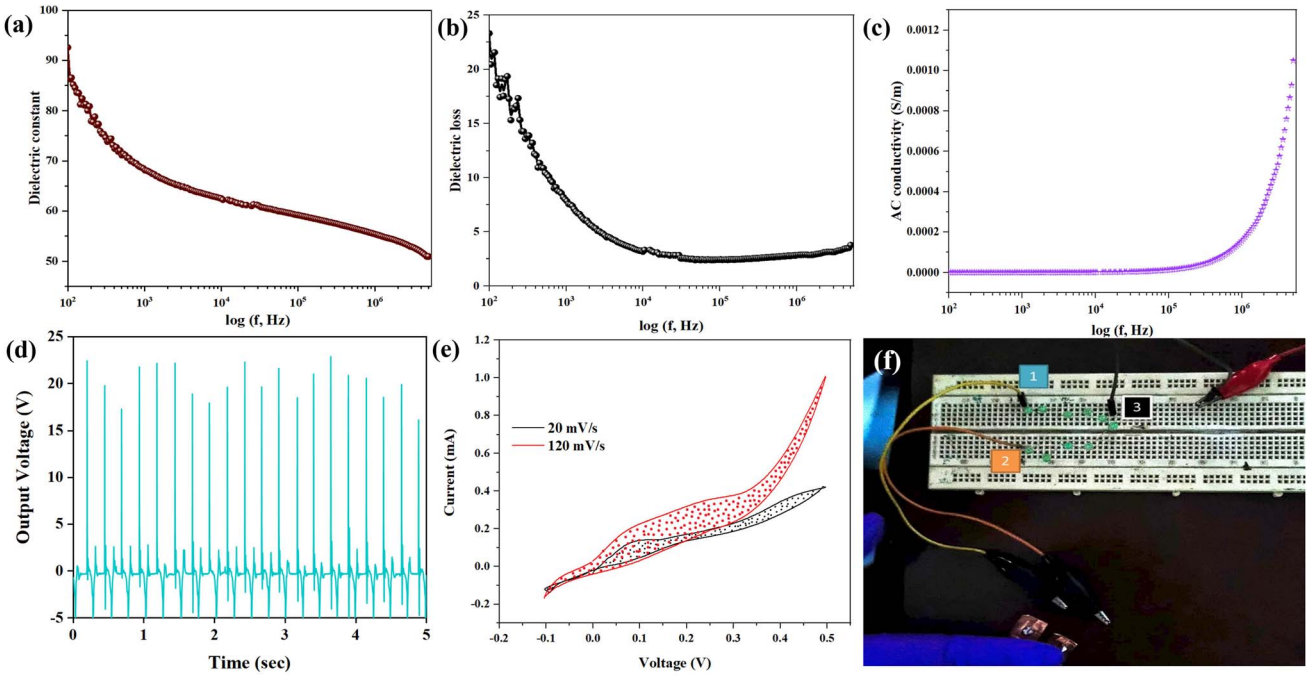

Fig. 9 (a) Dielectric constant, (b) dielectric loss, and (c) AC conductivity of multilayer E-FS; (d) voltage output of multilayer E-FS upon finger tapping recorded using a digital oscilloscope; (e) CV of multilayer E-FS; (f) circuit analysis of piezo properties of both the aligned PVDF and E-FS, showing LED blinking when the sensor is tapped.

inputs can be effectively converted into electrical signal towards energy harvesting or wearable sensor technologies.

3.17. Device fabrication

In this experimental setup (Fig. 9f), a piezoelectric sensor composed of aligned PVDF nanofibers and E-FS is externally connected to a breadboard circuit *via* alligator clips. The positive and negative terminals of the sensor are connected to the circuit at designated points (labelled 1 and 2), with a common ground (labelled 3) serving as the reference potential. Mechanical stimulation is applied to the sensor through palm tapping, which induces voltage spikes due to the piezoelectric effect of the PVDF material. These voltage signals are sufficient to momentarily forward-bias a series of green LEDs on the breadboard, causing them to blink in synchronization with each tap. This response confirms the sensor's ability to convert mechanical stimuli into electrical signals, demonstrating its potential for use in tactile sensing and biomedical applications.

The integration of β-PVDF nanofibers with demineralized fish scales resulted in a multi-layered, flexible, and bioactive collagen-based matrix that retained native anisotropy to facilitate cellular alignment.[48,49] The removal of mineral phases, primarily hydroxyapatite, yields a collagen-rich, flexible matrix that closely resembles the architecture of native soft tissue matrices. This demineralization process significantly enhances FS porosity and nutrient permeability, thereby facilitating superior cell infiltration and tissue integration, as confirmed by a series of biological assays, including cytotoxicity, hemocompatibility, and LIVE/DEAD assessments. As this study is primarily aimed at developing biologically functional scaffolds for tissue regeneration rather than energy harvesting or sensing applications, an electrospinning technique was employed to achieve desirable fiber alignment and enhance the β-phase content in PVDF without the need for additional post-processing methods[50] thereby minimizing ECM degradation. In contrast, recently reported poling techniques produce a lower β-phase content in PVDF, making them more suitable for bulk applications like capacitors and transducers.[18] Notably, the voltage output measured from aligned PVDF fibers reaches approximately 28 V, which is several-fold higher than that achieved through the poling method, where the maximum output typically remains below 2 V. Therefore, the developed multilayer E-FS bio-template shows high impulse current with rapid discharge profile as bioelectric cues to guide stem cell fate towards regenerative medicine applications.

4. Conclusion

The demineralization of fish scales yielded a flexible, translucent collagen-based scaffold template that retained its native anisotropic structure for tissue engineering application. SEM analysis revealed the alignment of electrospun PVDF fibers with the specialised setup, while FTIR and XRD confirmed the presence of the β-phase, indicating the reason for their favourable structural and functional properties. The integration of β-PVDF nanofibers with demineralized fish scales resulted in a bi-layered, flexible, and bioactive collagen-based matrix that provides native anisotropy with significantly enhanced mechanical strength. Electrochemical and piezoelectric evaluations of the E-FS template revealed notable results, including a maximum voltage output of 15 V and a CV current ranging from 0.4 to 1.0 mA, highlighting its relevance to cellular stimulation. Owing to its tailorable

piezoelectric behaviour, biodegradability, cytocompatibility, and presence of a biocompatible β-PVDF layer, this hybrid biotemplate represents a promising smart biotemplate for various regenerative medicine applications.

Author contributions

Mr Samir Das: methodology, mechanical testing, biological assay, draft preparation. Ms Sri Medha Juloori: demineralization of fish scales, data curation, electrochemical analysis; Mr Mainak Swarnakar: piezoelectric analysis. Dr Manish Pal Chowdhury: review and editing. Prof. Santanu Dhara: conceptualization, study design, manuscript preparation, and finalization.

Conflicts of interest

The authors declare no conflicts of interest.

Note added after first publication

This article replaces the version published on 10th December 2025 in which Fig. 6 and 7 were inverted meaning the incorrect caption was associated with Fig. 6 and 7.

Data availability

The data that support the findings of this study are available from the corresponding author upon reasonable request.

Supplementary information (SI) is available. See DOI: https://doi.org/10.1039/d5su00448a.

Acknowledgements

The authors express their gratitude to the Indian Council of Medical Research (ICMR), Ministry of Textile, and the Prime Minister's Research Fellowship (PMRF) for their help in conducting this study. The authors express their gratitude to the Institutional Animal Ethics Committee of IIT Kharagpur, CRF at IIT Kharagpur, and all the staff of Biomaterials and Tissue Engineering (BMTE) lab. The authors would like to acknowledge Mr Krishnabrata Panda and Mr Nantu Dogra for helping with the experiments.

References

1 A. Jana and A. Chattopadhyay, Prevalence and potential determinants of chronic disease among elderly in India: rural-urban perspectives, *PLoS One*, 2022, **17**(3), e0264937.
2 I. Sallent, *et al.*, The few who made it: commercially and clinically successful innovative bone grafts, *Front. Bioeng. Biotechnol.*, 2020, **8**, 952.
3 R. Davis, *et al.*, A comprehensive review on metallic implant biomaterials and their subtractive manufacturing, *Int. J. Adv. Manuf. Technol.*, 2022, **120**(3), 1473–1530.
4 H. Shi, C. Wang and Z. Ma, Stimuli-responsive biomaterials for cardiac tissue engineering and dynamic mechanobiology, *APL Bioeng.*, 2021, **5**(1), 011506.
5 G. Singh and A. Chanda, Mechanical properties of whole-body soft human tissues: a review, *Biomed. Mater.*, 2021, **16**(6), 062004.
6 A. D. Theocharis, D. Manou and N. K. Karamanos, The extracellular matrix as a multitasking player in disease, *FEBS J.*, 2019, **286**(15), 2830–2869.
7 Y. Zhao, *et al.*, Periosteum-bone inspired hierarchical scaffold with endogenous piezoelectricity for neuro-vascularized bone regeneration, *Bioact. Mater.*, 2025, **44**, 339–353.
8 D. Qin, *et al.*, Natural micropatterned fish scales combing direct osteogenesis and osteoimmunomodulatory functions for enhancing bone regeneration, *Composites, Part B*, 2023, **255**, 110620.
9 A. H. Rajabi, M. Jaffe and T. L. Arinzeh, Piezoelectric materials for tissue regeneration: A review, *Acta Biomater.*, 2015, **24**, 12–23.
10 L. Salvatore, *et al.*, Mimicking the hierarchical organization of natural collagen: toward the development of ideal scaffolding material for tissue regeneration, *Front. Bioeng. Biotechnol.*, 2021, **9**, 644595.
11 M. S. Carvalho, *et al.*, Bone matrix non-collagenous proteins in tissue engineering: creating new bone by mimicking the extracellular matrix, *Polymers*, 2021, **13**(7), 1095.
12 T. Xiao, *et al.*, Biomimetic mineralization of collagen from fish scale to construct a functionally gradient lamellar bone-like structure for guided bone regeneration, *Int. J. Biol. Macromol.*, 2024, **281**, 136454.
13 Z. He, *et al.*, Electrospun PVDF nanofibers for piezoelectric applications: A review of the influence of electrospinning parameters on the β phase and crystallinity enhancement, *Polymers*, 2021, **13**(2), 174.
14 X. Wang, *et al.*, Unleashing the potential: strategies for enhancing performance of electrospun PVDF-based piezoelectric nanofibrous membranes, *Fibers Polym.*, 2024, **25**(11), 4075–4098.
15 G. Kalimuldina, *et al.*, A review of piezoelectric PVDF film by electrospinning and its applications, *Sensors*, 2020, **20**(18), 5214.
16 M. Satthiyaraju and T. Ramesh, Nanomechanical, mechanical responses and characterization of piezoelectric nanoparticle-modified electrospun PVDF nanofibrous films, *Arabian J. Sci. Eng.*, 2019, **44**, 5697–5709.
17 Y. Xi, F. Zhang and Y. Shi, Effects of surface micro-structures on capacitances of the dielectric layer in triboelectric nanogenerator: A numerical simulation study, *Nano Energy*, 2021, **79**, 105432.
18 N. D. Kulkarni, A. Saha and P. Kumari, Fabrication and testing of PVDF-Fish scales based sustainable piezoelectric impact sensor, *Sens. Actuators, A*, 2025, **382**, 116107.
19 S. W. Kang and J. Mueller, Adaptive core-shell 3D printing of hollow fiber actuators, *Device*, 2025, **3**(8), 100799.
20 S. Chuaychan, S. Benjakul and P. Nuthong, Element distribution and morphology of spotted golden goatfish fish scales as affected by demineralisation, *Food Chem.*, 2016, **197**, 814–820.
21 S. Gee, B. Johnson and A. L. Smith, Optimizing electrospinning parameters for piezoelectric PVDF nanofiber membranes, *J. Memb. Sci.*, 2018, **563**, 804–812.

22 K. Baltakys and T. Dambrauskas, Characterization of functional inorganic materials by X-ray diffraction methods, *FIM 2022: International Conference Functional Inorganic Materials 2022: Abstract Book*, Vilnius university press, 2022.
23 B. Zaarour, *et al.*, Controlling the secondary surface morphology of electrospun PVDF nanofibers by regulating the solvent and relative humidity, *Nanoscale Res. Lett.*, 2018, **13**(1), 285.
24 X. Cai, T. Lei, D. Sun and L. Lin, A critical analysis of the α, β and γ phases in poly (vinylidene fluoride) using FTIR, *RSC Adv.*, 2017, **7**(25), 15382–15389.
25 N. D. Kulkarni and P. Kumari, Development of highly flexible PVDF-TiO2 nanocomposites for piezoelectric nanogenerator applications, *Mater. Res. Bull.*, 2023, **157**, 112039.
26 A. Morali, A. Mandal, M. Skorobogatiy and S. Bodkhe, Unleashing the piezoelectric potential of PVDF: a study on phase transformation from gamma (γ) to beta (β) phase through thermal contact poling, *RSC Adv.*, 2023, **13**(44), 31234–31242.
27 M. Brzhezinskaya and V. E. Zhivulin, Controlled modification of polyvinylidene fluoride as a way for carbyne synthesis, *Polym. Degrad. Stab.*, 2022, **203**, 110054.
28 M. Sharma and A. Gaur, Fabrication of PVDF/BaTiO3/NiO nanocomposite film as a separator for supercapacitors, *J. Energy Storage*, 2021, **38**, 102500.
29 Q. Ye, *et al.*, Chain orientation-dependent polymorphic crystallization of poly (vinylidene fluoride): a guide to achieving polar phases, *Macromolecules*, 2024, **57**(8), 3671–3686.
30 A. K. Maurya, *et al.*, Understanding multiscale structure–property correlations in PVDF-HFP electrospun fiber membranes by SAXS and WAXS, *Nanoscale Adv.*, 2022, **4**(2), 491–501.
31 N. D. Kulkarni and P. Kumari, Role of rGO on mechanical, thermal, and piezoelectric behaviour of PVDF-BTO nanocomposites for energy harvesting applications, *J. Polym. Res.*, 2023, **30**(2), 79.
32 M. Kumar, N. D. Kulkarni and P. Kumari, Fabrication and characterization of PVDF/BaTiO3 nanocomposite for energy harvesting application, *Mater. Today Proc.*, 2022, **56**, 1151–1155.
33 M. Georgiadis, R. Müller and P. Schneider, Techniques to assess bone ultrastructure organization: orientation and arrangement of mineralized collagen fibrils, *J. R. Soc. Interface*, 2016, **13**(119), 20160088.
34 S. J. Akinbodunse, *et al.*, Evaluation of the Rietveld method for determining content and chemical composition of inorganic X-ray amorphous materials in soils, *Am. Mineral.*, 2024, **109**(12), 2037–2051.
35 D. Qin, *et al.*, Development and application of fish scale wastes as versatile natural biomaterials, *Chem. Eng. J.*, 2022, **428**, 131102.
36 E. P. Paschalis, S. Gamsjaeger and K. Klaushofer, Vibrational spectroscopic techniques to assess bone quality, *Osteoporosis Int.*, 2017, **28**(8), 2275–2291.
37 Y. Tan, Heterogeneous Distribution and Corresponding Mechanical Significance of The Mineral Phase in Fish Scales, Master thesis, Diss. Virginia Tech, 2023, http://hdl.handle.net/10919/114111.
38 C. Balaji Ayyanar and K. Marimuthu, Investigation on the morphology, thermal properties, and in vitro cytotoxicity of the fish scale particulates filled high-density polyethylene composite, *Polym. Polym. Compos.*, 2020, **28**(4), 285–296.
39 A. Ghosh, S. S. Ray, J. T. Orasugh and D. Chattopadhyay, Collagen-Based Hybrid Piezoelectric Material, *Hybrid Mater. Piezoelectric Energy Harvest. Convers.*, 2024, pp. 283–299.
40 H.-P. Li, *et al.*, Influence of β-phase content on the stretching-induced α-β phase transition of highly oriented poly (vinylidene fluoride) ultrathin films, *Chin. J. Polym. Sci.*, 2025, 1–9.
41 A. S. Motamedi, H. Mirzadeh, F. Hajiesmaeilbaigi, S. Bagheri-Khoulenjani and M. Shokrgozar, Effect of electrospinning parameters on morphological properties of PVDF nanofibrous scaffolds, *Prog. Biomater.*, 2017, **6**, 113–123.
42 S. Mohammadpourfazeli, *et al.*, Future prospects and recent developments of polyvinylidene fluoride (PVDF) piezoelectric polymer; fabrication methods, structure, and electro-mechanical properties, *RSC Adv.*, 2023, **13**(1), 370–387.
43 H. Quan, W. Yang, M. Lapeyriere, E. Schaible, R. O. Ritchie and M. A. Meyers, Structure and mechanical adaptability of a modern elasmoid fish scale from the common carp, *Matter*, 2020, **3**(3), 842–863.
44 S. Kundu, *et al.*, The formation of nitrogen-containing functional groups on carbon nanotube surfaces: a quantitative XPS and TPD study, *Phys. Chem. Chem. Phys.*, 2010, **12**(17), 4351–4359.
45 E. P. Motta, J. M. L. Reis and H. S. da Costa Mattos, Analysis of the cyclic tensile behaviour of an elasto-viscoplastic polyvinylidene fluoride (PVDF), *Polym. Test.*, 2018, **67**, 503–512.
46 A. Saha, N. D. Kulkarni, M. Kumar and P. Kumari, The structural, dielectric, and dynamic properties of NaOH-treated Bambusa tulda reinforced biocomposites—an experimental investigation, *Biomass Convers. Biorefin.*, 2024, **14**(20), 26247–26266.
47 L. Rohmawati, W. Setyarsih and T. Nurjannah, Variation sweep rate cyclic voltammetry on the capacitance electrode activated carbon/PVDF with polymer electrolyte, *J. Phys.: Conf. Ser.*, 2018, **997**(1).
48 J. A. Reid, *et al.*, Architected fibrous scaffolds for engineering anisotropic tissues., *Biofabrication*, 2021, **13**(4), 045007.
49 S. Dhara, *et al.*, Ethically sourced biotemplate engineered with smart polymer for promoting skeletal tissue regeneration, *MRS Commun.*, 2025, 1–10.
50 F. Mokhtari, *et al.*, Recent progress in electrospun polyvinylidene fluoride (PVDF)-based nanofibers for sustainable energy and environmental applications, *Prog. Mater. Sci.*, 2024, 101376.